ORIGINAL ARTICLE
Journal Section

Analysis of the 3D microstructure of experimental cathode films for lithium-ion batteries under increasing compaction

Klaus Kuchler[1] | Benedikt Prifling[1] | Denny Schmidt[2] | Henning Markötter[4] | Ingo Manke[4] | Timo Bernthaler[3] | Volker Knoblauch[3] | Volker Schmidt[1]

[1]Institute of Stochastics, Ulm University, 89069 Ulm, Germany

[2]Robert Bosch Battery Systems GmbH, 70469 Stuttgart, Germany

[3]Materials Research Institute, Aalen University, 73430 Aalen, Germany

[4]Institute of Applied Materials, Helmholtz-Zentrum Berlin, 14109 Berlin, Germany

Correspondence
Benedikt Prifling, Institute of Stochastics, Ulm University, 89069 Ulm, Germany
Email: benedikt.prifling@uni-ulm.de
Phone: 0731 5023555
Fax: 0731 5023649

It is well known that the microstructure of electrodes in lithium-ion batteries has an immense impact on their overall performance. The compaction load during the calendering process mainly determines the resulting morphology of the electrode. Therefore, NCM-based cathode films from uncompacted (0 MPa) to most highly compacted (1000 MPa) were manufactured, which corresponds to global porosities ranging from about 50% to 18%. All samples have been imaged using synchrotron tomography (TXM). This image data allows an extensive analysis of the 3D cathode microstructure with respect to increasing compaction. In addition, the numerous microstructural changes can be quantified using several characteristics describing the morphology of cathode samples. Three characteristics, namely global porosity, global volume fraction of active material and mean cathode thickness, are compared to experimental results. In addition, the microstructural analysis by means of 3D image data and image processing techniques allows the investigation of characteristics which are hard or impossible to ascertain by experiments, for example the continuous pore size distribution and the sphericity distribution of NCM-particles.

Finally, the dependency of microstructural characteristics on compaction load is described by the help of parametric probability distributions. This approach can be used, for example, to predict the distribution of a certain characteristic for an “unknown” compaction load, which is a valuable information with regard to the optimization and development process of NCM-cathodes in lithium-ion batteries.

1 | INTRODUCTION

Lithium-ion batteries play a major role in a wide field of applications ranging from electric vehicles to mobile phones. In addition, lithium-ion batteries combine a couple of preferable properties as, for example, a relatively low self-discharge rate as well as a high energy density. As shown in Wiedemann et al. (2013), García et al. (2005), Huang et al. (2009), Cho et al. (2015), Wang et al. (2017), Li and Currie (1997) and Shin and Manthiram (2004), the morphology of the electrodes mainly influences the overall battery performance. For example, it is shown in Röder et al. (2016) that the agglomeration of active material particles can decrease the capacity of the electrode. Therefore, a deeper understanding of the 3D microstructure of cathodes as well as anodes is an important task in order to optimize the functionality of lithium-ion batteries. In recent years, the systematic structuring of electrodes has become more and more import in battery research, see Wang et al. (2012), Song et al. (2010) and Vu et al. (2012). The cathode manufacturing process, which involves, among others, mixing, coating, drying or calendering, strongly influences the electrochemical performance, see Bockholt et al. (2013), Lenze et al. (2017), Lenze et al. (2018) and Bockholt et al. (2016). For example, the electrical pathways can be improved, among others, by adding graphite or calendaring, see Bockholt et al. (2016).

In the present paper, we will focus on eight experimentally manufactured cathodes described in Schmidt et al. (2018), which have been densified with different compaction loads ranging up from0 MPa to 1000 MPa. The calendering process is of great interest with regard to the functionality of the lithium-ion battery, since it mainly determines the cathode morphology and hence several characteristics, as for example electrode thickness and global porosity and thus energy and power density, see Gnanaraj et al. (2001), Zheng et al. (2008), Haselrieder et al. (2013) and Zheng et al. (2012). A detailed analysis of the calendering process can be found in Meyer et al. (2017). In order to quantitatively investigate the influence of the compaction load on the cathode microstructure, the 3D information of eight differently compacted cathodes has been obtained using synchrotron tomography, which allows non-destructive imaging combined with high resolution. Considering 3D instead of 2D images has the advantage that spatially localized features, which mainly influence the overall battery functionality (see Waldmann et al. (2016) and Zhang et al. (2011)), can be taken into account. In addition, the detailed microstructure analysis in Section 3 provides valuable information regarding the electrochemical performance.

At this point, an outline of the subsequent sections is given. In Section 2 material, manufacturing and compaction of the considered NCM-cathode films is discussed in detail. Additionally, it is briefly explained how microstructural characteristics like porosity were experimentally determined. Then a short overview of the sample preparation and tomographic imaging procedure follows. In order to be able to perform an extensive analysis including several microstructural characteristics, the tomographic image data is preprocessed, see Section 3.1. The results of the quan-

titative analysis of preprocessed 3D microstructures of the compacted cathodes are presented in Sections 3.2 and 3.3, respectively. Section 3 also contains comparisons between results for characteristics determined by 3D image data and experimental measurements. In addition, the distributions of microstructural characteristics can be modeled using suitable parametric probability distributions. Therefore, we can use classical regression analysis in order to quantitatively investigate the relationship between the compaction load and the corresponding parameters, which is performed in Section 4. In this way, we are able to predict the distributions of microstructural characteristics for an arbitrary compaction load. Finally, the obtained results and conclusions are summarized in Section 5.

2 | SAMPLE PREPARATION AND TOMOGRAPHIC IMAGING

In this section, the material composition of the considered cathode films and their manufacturing and compaction processes is described. Then, an explanation of the preparation of samples of these cathode films for tomographic imaging purposes follows. The tomographic imaging procedure itself is briefly described as well.

2.1 | Cathode manufacturing

The cathode samples were manufactured with $LiNi_{1/3}Co_{1/3}Mn_{1/3}O_2$ (NCM111) as active material (92 wt%), polyvinyliden fluorid (PVdF) as binder (4 wt%) and carbon-based conductive additives, i.e. carbon black (2 wt%) and graphite (2 wt%). The absolute density of each component was determined by a He-pycnometer AccuPyc 1330 (Micromeritics): NCM111: $4.7\,g/cm^3$; PVdF: $1.77\,g/cm^3$, conductive additives: $2.26\,g/cm^3$. The absolute density of the mixed powder was calculated with regard to the final composition with $4.13\,g/cm^3$. The basis of the cathode slurry was N-methyl-2-pyrrolidon (NMP), an organic solvent. At the first, the binder has been dissolved at 800 rpm for at least 60 minutes. Afterwards, the following components have been added and mixed by using a mechanical dissolver: Carbon black (2000 rpm, $\geq$ 45 minutes), graphite (1500 rpm, $\geq$ 30 minutes) and finally active material (2000 rpm, $\geq$ 120 minutes). The specified mixing times have been met to ensure a homogeneous distribution of the solid components and to dissolve agglomerates. Following this, a 15 μm thick aluminum foil was coated with slurry by using the doctor blade method with a constant speed of 2 cm/s. The slot height of the coating tool was adjusted by 275 μm, that is equal to the wet film thickness. The subsequent drying process took place at room temperature in a fume hood for at least 12 hours. The cathode dryness has been tested using Karl Fischer titration, which resulted in a moisture content of 480 ppm. The allover distributed solvent evaporated and generated the pores or rather the pore network within the active mass, which consists of active material, binder and conductive additives. Circular samples with a diameter of 10 mm were cut by precision cutting tool (Nogamigiken). The weight of cathode samples (active mass plus aluminum foil) was measured by microgram scale (Satorius). To realize different compaction loads, the samples were densified under uniaxial compression by universal testing machine RSA 100 (Schenk) between two surface-polished and ball bearing mounted press tools with compaction loads of 100, 200, 300, 400, 500, 750 and 1000 MPa in a quasi-static mode. The dry film thickness of the uncompacted (corresponds with 0 MPa) and various compacted cathode samples was determined by a micrometer caliper (Mitutoyo). This information allows us to determine the total volume of the cathode sample for each compaction load, which is combined with the total weight in order to compute the overall absolute density of the cathode sample. Finally, the proportion of weight of each solid component allows us to calculate the overall porosity, the volume fraction of NCM-particles as well as the volume fraction of binder and conductive additives for each considered compaction load. These experimentally determined characteristics will be compared to the results of 3D image analysis in Section 3.

2.2 | Sample preparation

To be able to investigate the influence of the compaction load on the morphology of the considered cathodes by means of 3D imaging procedures, the electrodes had to be appropriately prepared. Therefore, single circular electrodes (diameter 10 mm, coated one-sided) were alternatingly placed between Kapton polyimide films (self-adhesive). This way, two stacks, each containing four differently compacted cathode films, were built as illustrated in Figure 1. Finally, one thin strip (width 1.5 mm) was cut by a scalpel from the stacks with circular electrodes each, which have been used for the tomographic imaging procedure described in Section 2.3. To stabilize the sample stack during measurement it was embedded in resin within a capton tube with 1.6 mm diameter. Note that the previous steps might lead to slight changes of the microstructure at the cut surface. Therefore, the quantitative analysis in Section 3 is based on smaller observation windows in the inner part of the sample in order to avoid edge-effects.

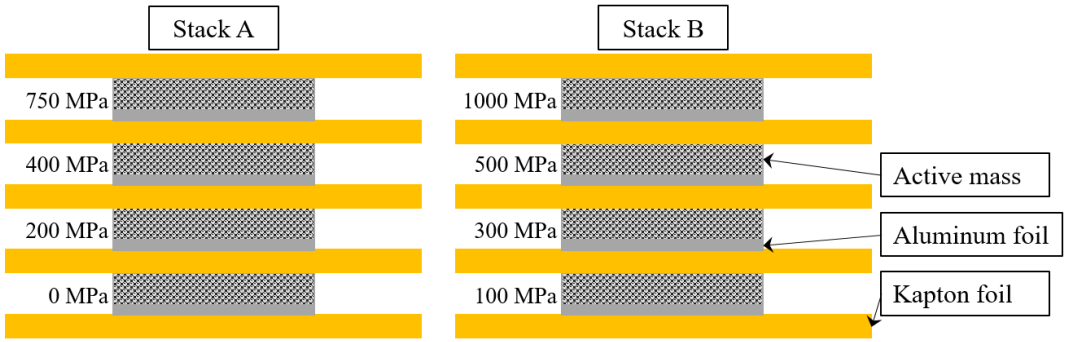

FIGURE 1 Illustration of the setup of both sample stacks surrounded by Kapton polyimide films. Different compaction rates are declared next to single-sided coated cathode samples.

2.3 | Tomographic imaging procedure

The prepared sample stacks, see Section 2.2, were tomographically measured at the synchrotron X-ray facility BAM-line at BESSY *II* in Berlin, Germany. Synchrotron tomography, or more precisely X-ray transmission tomography (TXM), allows a non-destructive and high-resolution imaging of the cathode microstructures in the prepared stacks. By rotation of the sample stacks while recording projection images the 3D structure can be reconstructed. One tomographic scan was conducted collecting 2200 projections during a sample rotation of 180 degree within a total scan time of approximately 2 hours. A photon energy of 25 keV and a detector distance of 10 mm allowed for sufficient transmission through the samples while obtaining an adequate contrast of the active material. 3D volume reconstruction was conducted via filtered back projection. Image normalization and reconstruction was done with self-written code in *IDL (Exelis Visual Information Solutions, Boulder, Colorado)*. Finally, the tomographically scanned cathode films for the eight compaction loads have been provided in a 16-bit grayscale image format. Cutouts of the uncompacted cathode and the 300 MPa compacted cathode are shown in Figure 2. Note that the voxel size is $0.44 \times 0.44 \times 0.44\,\mu$m.

However, one drawback of the tomographic measurements is that we cannot distinguish between pores and non-active material which consists of binder and conductive additives, see Section 2.1. This means that the "darker background" in the grayscale images is actually composed of pores, binder and conductive additives, which is called the binder-additives-pore phase, shortly bap-phase. Therefore, missing (non-separable) binder and conductive additives are artificially added to image data by a, from our point of view, reasonable approach, see Section 3.1. The phase of NCM-particles ("brighter foreground" in the grayscale images) is called the active material phase, shortly am-phase. Due to the previously described step, the cathode microstructure is modeled using three phases (active material, pores and conductive additives plus binder) instead of two (active material and bap-phase), which allows a more realistic and accurate description of the morphology.

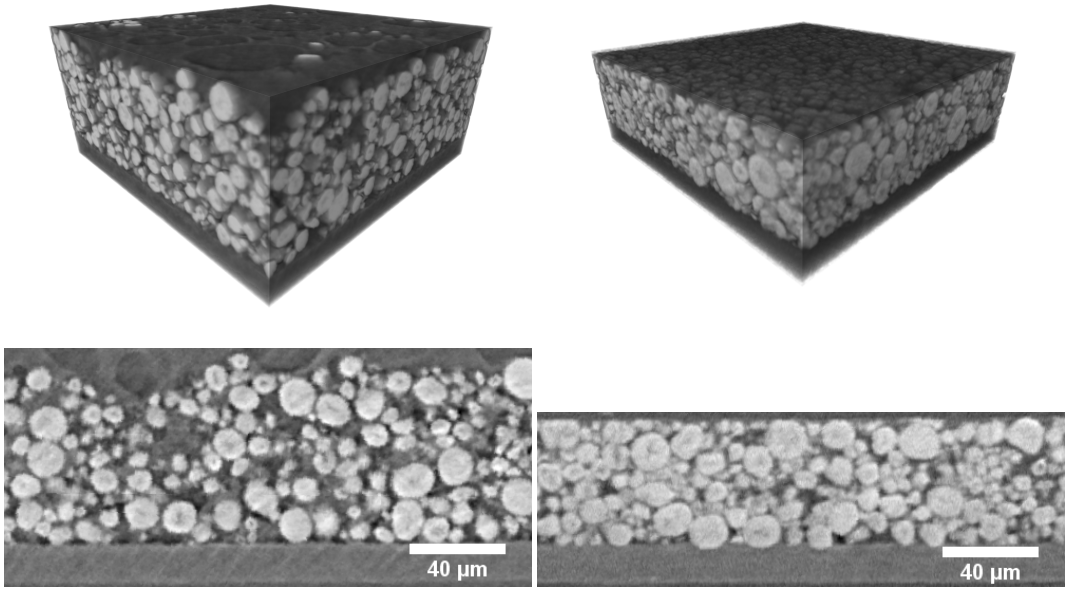

FIGURE 2 Visualization of the microstructure of the uncompacted cathode (left column) and the 300 MPa compacted sample (right column), i.e. three-dimensional renderings (first row) and through-plane cross sections of tomographically measured cathode films as 16-bit grayscale images (second row).

3 | QUANTITATIVE ANALYSIS OF 3D MICROSTRUCTURE

In this section, we quantitatively analyze the influence of increasing compaction loads on the 3D morphology of experimentally manufactured cathodes described in Section 2. All subsequent results in this section are based on 3D image data gathered by synchrotron tomography, see Section 2.3. To perform a quantitative analysis of the 3D microstructure based on 3D image data, it is necessary to preprocess image data in several steps. Afterwards, we focus on phase-based characteristics using the definition of phases introduced in Section 2.3. Finally, we determine particle-based characteristics using the 3D integer-labeled image data described in Section 3.1.

Note that the experimental manufacturing process of cathodes is by nature subject to inhomogeneities. This fact causes slight fluctuations and discontinuities in some considered characteristics. Furthermore, presented experimental results are based on measurements of several cathodes for each considered compaction load, whereas results of 3D image data analysis are only based on one cathode sample for each considered compaction rate. This fact can be a possible explanation for slightly different values between experimental results and results obtained from 3D image data.

3.1 | Preprocessing of image data - phase and particle segmentation

In order to attain appropriate phase-segmented and particle-segmented (integer-labeled) image data, it is essential to preprocess the grayscale image data described in Section 2.3. As a first step, the tomographically measured cathode films are initially rotated and then straightened using polynomial regression to obtain nearly planar cathode films. The current collector at the bottom of each cathode film, see Figure 2, is separated from the remaining sample. To reduce noise in the tomographic grayscale images, a 3D median filter with a ball of radius 1 as structuring element is applied to image data, see e.g. Burger and Burge (2016). By using a global threshold ℓ, the filtered image is now segmented into two phases, am-phase (NCM-particles) and bap-phase (binder, conductive additives and pores), respectively. The results are shown in Figure 3. The threshold ℓ is chosen in such a way that the volume fraction of the am-phase of each considered cathode film computed from 3D image data closely coincides with the known volume fraction of am-phase. For this purpose, a sufficiently large observation window within the cathode sample was used in order to avoid edge effects. The volume of those cuobids is given in Table 1. The numerical values for the global threshold ℓ range from 45158 to 47446.

comp. load [MPa]	0	100	200	300	400	500	750	1000
Volume used for global thresholding [10^6 voxel]	491	528	459	389	407	357	365	315
Total volume [10^6 voxel]	1083	1043	866	892	810	807	777	719

TABLE 1 Volume of the observation window, which is used for estimating the global threshold ℓ, as well as size of the whole sample for each compaction load.

Note that phase segmentation results were also visually inspected by checking whether the am-phase hits the boundaries of the NCM-particles in the grayscale images appropriately. Afterwards, 12 preferably homogeneous and disjoint (i.e., non-overlapping) cutouts have been extracted from the binarized cathode film. Each cutout has a size of 500×500 voxels ($219\,\mu\text{m} \times 219\,\mu\text{m}$) in horizontal direction (in-plane) and the corresponding thickness of the cathode film in vertical direction (through-plane).

To finalize phase segmentation, two amendment steps were additionally performed beginning with a removal of small bap-phase clusters (e.g. pores) followed by a removal of small am-phase clusters (particle fragments). For both, the Hoshen-Kopelman clustering algorithm (see Hoshen and Kopelman (1976)) has been applied to detect clusters of the bap- and am-phase, respectively. All voxels of detected am-phase clusters with a size less than 300 voxels were set to the bap-phase, because such small am-phase parts usually are artifacts from sample preparation or tomographic imaging. It can be assumed that these small parts are no particles or negligibly small fragments of NCM-particles. Analogously, all voxels of the detected bap-phase clusters consisting of less than 5000 voxels were set to the am-phase. By doing this, the internal porosity of NCM-particles, which might cause an over-segmentation of some particles, can be eliminated. Note that this parameter is more than one order of magnitude larger than the corresponding parameter

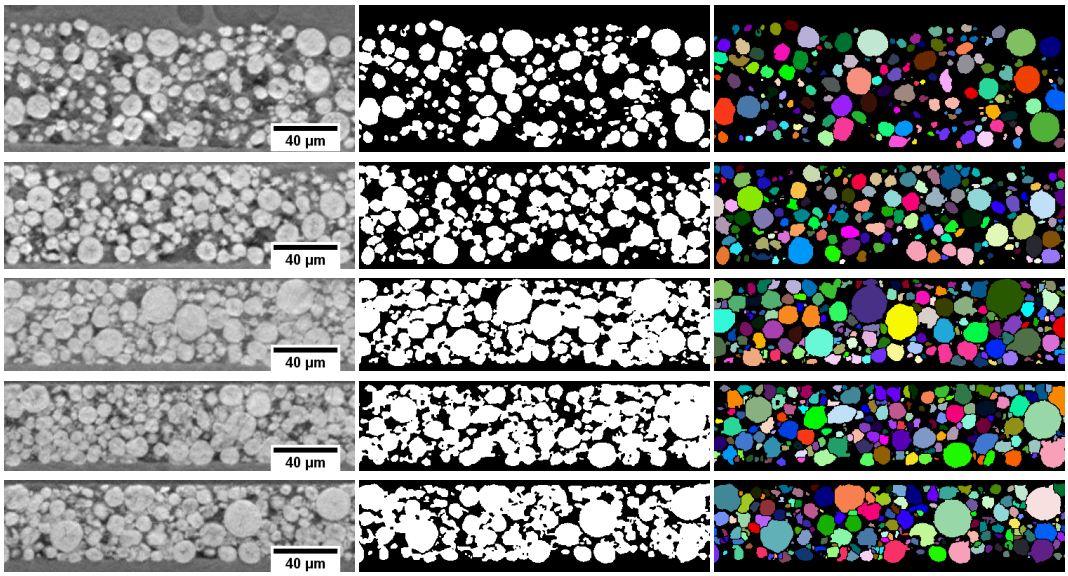

FIGURE 3 Through-plane cross sections of cathode microstructure for compaction loads 0, 100, 400, 750 and 1000 MPa (from top to bottom). Left column: original 16-bit grayscale; middle column: phase-segmented; right column: particle-segmented.

for am-phase clusters, since it is possible that NCM-particles contain comparatively large wholes inside.

For the purpose of a particle-based analysis of the compacted cathodes it is essential that single particles are extracted from the previously phase-segmented image data. We can realize this intention quite well by using a marker-based watershed algorithm, see e.g. Beucher and Meyer (1993). Especially for the less strongly compacted cathodes this approach leads to excellent results, whereas it becomes more difficult to correctly identify single particles in highly-dense microstructures of cathodes corresponding to a compaction load of > 300 MPa. Hence, the most important issue to solve is to define a suitable set of markers from which such a watershed algorithm may start. At first, the inverted Euclidean distance transform from am-phase to bap-phase is computed. Based on this 3D image, we detected regional minima, i.e. neighboring voxels with the same negative value whose directly surrounding voxels have larger values.

Afterwards, so-called extended regional minima are constructed, see Spettl et al. (2015). That is, an existing regional minimum is extended by adjacent voxels whose corresponding values in the inverted Euclidean distance transform do not differ by more than $\varepsilon(d_{\min})$ from the value $d_{\min}$ of the existing regional minimum. This "epsilon-value" $\varepsilon(d_{\min})$ locally depends on $d_{\min}$ and is chosen as $\varepsilon(d_{\min}) = \max\{|f \cdot d_{\min}|, \varepsilon\}$, where $f, \varepsilon \geq 0$. A careful choice of these two parameters leads to a nice merging of some previously adjacent regional minima in order to reduce over-segmentation. The remaining minima, which represent in general regions of neighboring voxels, form a set of markers.

The set of markers described above has been used to start the so-called "flooding" in the marker-based watershed algorithm. Starting from every marker (region) placed in the inverted Euclidean distance transform relief, the "basins" (or rather "valleys") are progressively flooded and "watersheds" are constructed where different flooded "basins" meet. Further information regarding the watershed algorithm can be found in Beare and Lehmann (2006); Beucher and Meyer (1993). The result of this segmentation procedure is an integer-labeled image where all voxels of an identified

single particle (segmented domain) are assigned to a unique positive integer, whereas all bap-phase voxels as well as voxels of the “watersheds” (transient area between segmented domains) have the value zero.

To further improve segmentation by reducing over-segmentation, we applied a post-segmentation step as it has been also performed in Kuchler et al. (2018). In this post-segmentation step all so far segmented particles (from the above segmentation) are dilated by a ball of some radius $r_{post} \geq 0$ and then it is checked whether a dilated particle completely overlaps an adjacent original (undilated) particle. If that also holds in the reverse case, then only the marker of the originally smaller particle is removed and otherwise just the marker of the overlapped particle is removed from the set of markers. With the resulting subset of markers we redo the marker-based watershed algorithm and obtain the final particle segmentation as shown in the right column of Figure 3. Note that radii r_{post} ranging from 6 up to 8 voxels were applied.

Recall that in the tomographic images we cannot distinguish between pores, binder and conductive additives which had ended up in the compound bap-phase. From material composition of the solid components and their absolute densities, see Section 2.1, it is known that the volume of NCM-particles corresponds to 83 % of the cumulative volume of all solid components. Thus, 17 % volume of the active mass are not visible in image data and this is exactly the target volume V_{ba} of binder and conductive additives which has to be inserted into bap-phase. In other words, some voxels originally belonging to bap-phase (value 0) are now considered as voxels belonging to binder and conductive additives (new value 128) by performing a morphological closing of the am-phase. For further information on morphological closing we refer to Soille (2003). The structuring element is a ball whose radius r_{close} is determined by a bisection method. The bisection method yields a radius r_{close} such that the volume of artificially added binder and conductive additives is slightly larger than V_{ba}. In order to exactly match the target volume V_{ba}, the volume of the binder and additives is iteratively reduced by randomly resetting voxels with value 128 to voxels with value 0 (pore phase). An example of how binder and conductive additives are artificially added to phase-segmented image data is shown in Figure 4. The phase consisting of binder and conductive addititves is more or less homogeneously distributed between the NCM-particles as one might expect and as shown in Weisenberger et al. (2014).

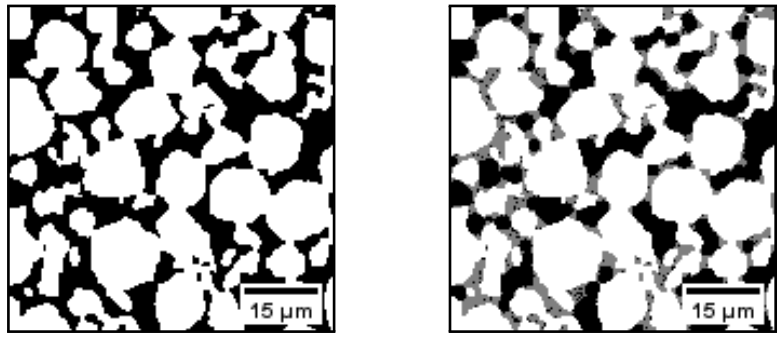

FIGURE 4 Two-dimensional cutouts of phase-segmented cathode microstructure for compaction load 300 MPa. Left: Binarized image consisting of NCM-particles and bap-phase. Right: Grayscale image after artificially adding binder and conductive additives (gray).

After phase and particle segmentation, we have a sufficiently rich data basis for an extensive quantitative analysis of the morphology of each cathode film. For the purpose of a meaningful comparability of the compacted cathodes, all considered microstructural characteristics, both phase- and particle-based, were determined based on the corresponding 12 cutouts and then combined to obtain averaged results. As already mentioned, these cutouts have a

size of $500 \times 500 \times z$ voxels which corresponds to $219 \times 219 \mu m^2$ in in-plane direction, where z denotes the specific number of slices in through-plane direction. Note that at this point, each of these cutouts also contains void space surrounding the cathode sample. The actual thickness t of each considered sample was determined experimentally by a micrometer caliper (Mitutoyo), see Schmidt et al. (2018). In addition, we used the binarized 3D synchrotron images to determine the mean cathode thickness by means of a rolling ball, i.e. a method based on a morphological closing, see Machado Charry et al. (2018). Table 2 shows a high accordance between these two approaches except for the uncompacted cathode, where we want to point out that the experimental values are always larger compared to the approach based on 3D image data. This might be caused by the sample preparation described in Section 2.2 since each cathode is additionally compacted during the preparation of the sample stack leading to a minor reduction of the cathode thickness.

comp. load [MPa]	0	100	200	300	400	500	750	1000
experimental [μm]	79.8	61.0	57.2	53.7	51.9	51.0	49.8	49.1
image data [μm]	72.4	59.9	55.6	52.1	51.7	49.7	49.2	47.3

TABLE 2 Mean cathode thickness t of each compacted cathode film (without current collector) based on image data and experimental measurements.

3.2 | Phase-based characteristics of active material and pore phase

In this section we focus on the analysis of phase-based characteristics, where edge correction is used in order to obtain unbiased estimators. To begin with, we consider some first order characteristics like porosity, volume fraction of am-phase and specific surface area of am-phase, but also some more sophisticated characteristics like the so-called continuous pore size distribution (c-PSD) and a pore size distribution obtained from a virtually simulated mercury intrusion porosimetry (MIP-PSD). These two distributions (which are not cumulative probability distribution functions) make it possible to quantitatively analyze constrictivity, which allows us to characterize bottleneck effects in the compacted cathode microstructures. Additionally, we consider the so-called geodesic tortuosity which is calculated based on shortest path lengths through pore phase (see, e.g., Stenzel et al. (2016) and Stenzel et al. (2017)).

Due to our approach of artificially embedding binder and conductive additives into phase-segmented image data, it is also possible to determine the global porosity of compacted cathodes based on 3D image data. The global porosity is computed from 3D image data and then compared to experimental results obtained in Schmidt et al. (2018), see Figure 5a. Local porosities are computed in subwindows of size $50 \times 50 \times 50$ voxels, which are shifted through the corresponding large image cutout, where all cubic windows are non-overlapping. Figure 5b shows the evolution of locally computed porosities, where mean, standard deviation, minimum and maximum are depicted for each compaction load. The mean porosities, both global and local, computed from image data match the experimental results well. The standard deviation of locally computed porosities is quite small and nearly constant, beginning from the compaction load of 100 MPa, see Figure 5b. Thus, it can be concluded that the pore space is quite homogeneously spread over the compacted cathodes except for the uncompacted one. It is worth mentioning that global porosity based on 3D image data is always slightly smaller than the corresponding experimental porosity, which is not intuitive at first glance. However, this discrepancy might be explained by the fact that all characteristics based on 3D image data are determined using a smaller observation window in order to avoid edge effects, where the fissured “top” as

well as the “bottom” of the cathode film are not included. Of course, this issue has also to be taken into account when comparing the volume fractions of NCM-particles.

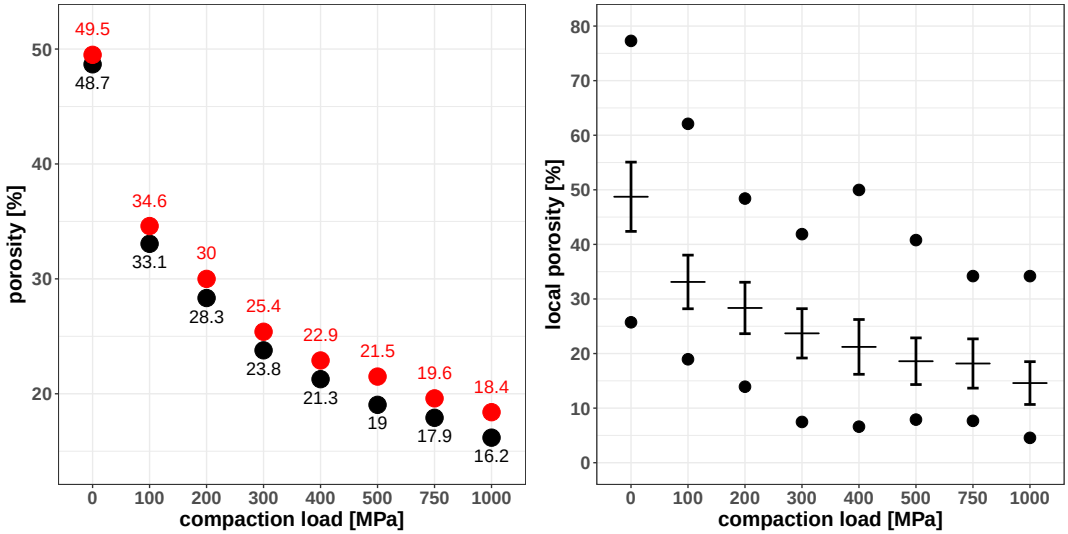

(a) Global porosity based on 3D image data (black) compared with experimental results (red), see Schmidt et al. (2018).

(b) Mean (dash), standard deviation (error bar), minimum and maximum (dots) of locally computed porosities.

FIGURE 5 Global porosity (left) and local porosities (right) of compacted cathodes as a function of the compaction load.

A second important characteristic we investigate is volume fraction of active material (NCM). As it can be seen in Figure 6a, there is a high accordance between the volume fractions of am-phase obtained from 3D image data and from experimental measurements, i.e. by volume measurements of the solid components using a He-pycnometer and additional knowledge about the proportion of weight of each component, see Schmidt et al. (2018). This indicates that the process of phase segmentation described in Section 3.1 is reasonable. Note however that the experimental values are always slightly smaller than the volume fractions based on image data, which is caused by the slight underestimation of experimental global porosity, see Figure 5a. In addition, the volume fraction of NCM-particles is monotonously increasing for increasing compaction as expected. Figure 6b also shows some characteristics concerning the distribution of local volume fractions of NCM particles. As it would be expected, the uncompacted cathode exhibits the largest standard deviation.

Furthermore, we look at the so-called specific surface area (SSA) of the am-phase, which is equal to the SSA of the bap-phase. We distinguish between the “classical” specific surface area, which is defined as the total surface area divided by the volume of the observation window, and the specific surface area per weight. The latter quantity is given by the surface area per unit of weight and can be determined using the detailed knowledge concerning the material composition, see Section 2.1. As it can be seen in Figure 7a, the specific surface area increases at first since the densification of the sample reduces the volume of the considered region of interest. Note that the considered volume in the denominator of the SSA is highly related to the thickness of the respective cathode film, see Table 2.

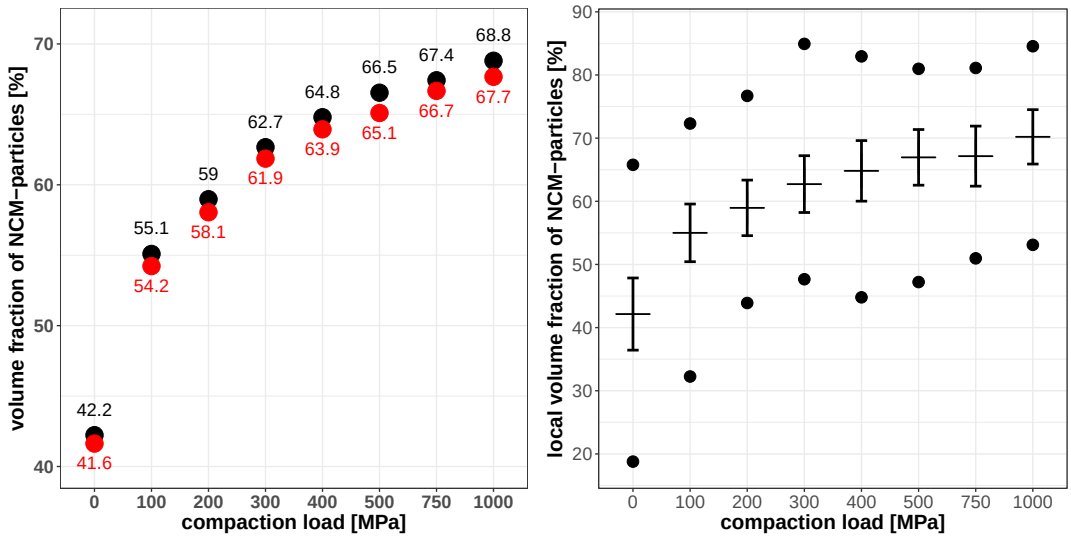

(a) Volume fraction of NCM-particles based on 3D image data (black) and based on volumetric measurements (red), see Schmidt et al. (2018).

(b) Mean (dash), standard deviation (error bar), minimum and maximum (dots) of locally computed volume fractions of NCM-particles based on 3D image data.

FIGURE 6 Global volume fraction of am-phase (left) and locally computed volume fractions of am-phase (right) as a function of the compaction load.

For compaction loads larger than 300 MPa the surface area of NCM-particles decreases inducing a slight decrease of the SSA. This might be caused by the fact that such high compaction loads lead to a lower number of "isolated" NCM-particles and a larger number of particles which share a common area of contact, i.e. clump together. At the same time, Figure 7b exhibits a strictly monotonous behavior of SSA per weight. A higher compacted cathode exhibits a higher bulk density and thus one unit of weight corresponds to a relatively small volume, which intuitively leads to a smaller surface area of NCM-particles. Once again, the most significant difference is observed between the uncompacted and the 100 MPa compacted cathode.

Subsequently, two more sophisticated characteristics are considered, namely, continuous pore size distribution and mercury intrusion porosimetry pore size distribution. The unnormalized c-PSD evaluated at a given radius r is given by the volume of the pore phase, which can be "filled" with (overlapping) balls of radius r. This concept incorporates pores that are not connected to the remaining pore network. Thus, c-PSD provides information on the distribution of pore sizes without any further constrictions, while MIP-PSD takes potential effects of bottlenecks through a direction-dependent pore size distribution into account. Note that virtual mercury intrusion porosimetry is simulated in through-plane direction starting from "separator side" to "current collector side" , i.e. from top to bottom in the sense of Figure 2. It is important to point out that c-PSD as well as MIP-PSD have been normalized by the total volume of the pore phase in order to obtain comparable results. Both characteristics provide valuable information concerning the geometry of transportation paths of lithium-ions since the morphology of the pore phase influences the electrochemical performance of lithium-ion batteries, see Lim et al. (2016). Further details regarding c-PSD and MIP-PSD can be found in Münch and Holzer (2008) and Holzer et al. (2013b).

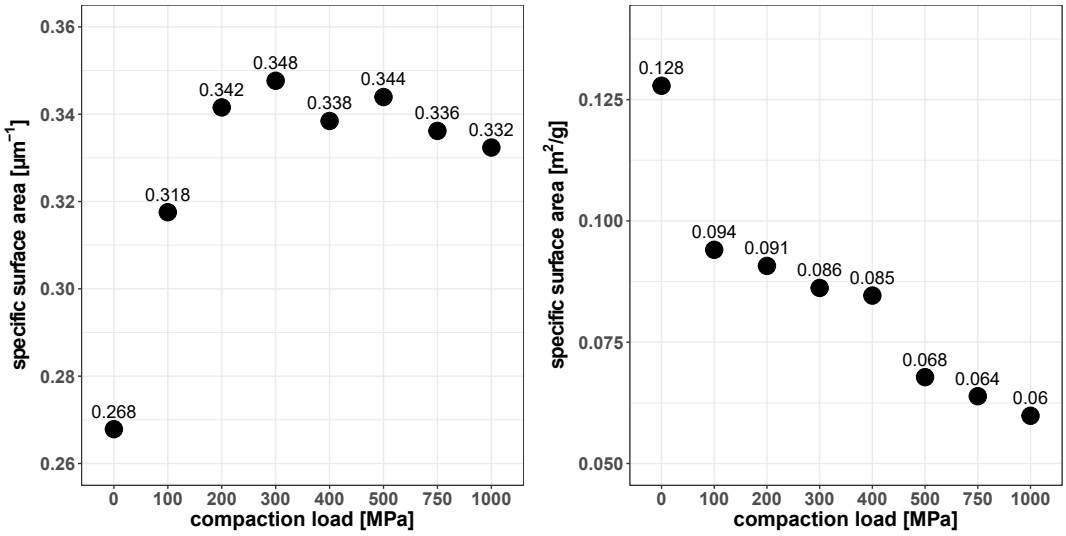

(a) Specific surface area of am-phase.

(b) Specific surface area per weight of am-phase.

FIGURE 7 Specific surface area (a) and specific surface area per weight (b) depicted for each considered compaction load, both based on 3D image data.

The evolution of both characteristics for increasing compaction loads is shown in Figure 8. With regard to c-PSD, see Figure 8a, one can observe that pores with radii larger than 4 μm already disappear after the first compaction step. Furthermore, it can be seen that there is a significant difference between 0 and 100 MPa, whereas higher compaction loads ($\geq$ 200 MPa) imply relatively small shifts of the c-PSD to the left. Next we focus on the investigation of the relationship between the compaction load and the MIP-PSD. A remarkable fact is that the pore radius for which we can observe a so-called "breakthrough" (i.e. significant jump in pore volume for marginally smaller radius) gets smaller for increased compaction, i.e., the typical diameter of bottlenecks is larger for less compacted cathodes. However, highly compacted cathodes ($\geq$ 300 MPa) have a less pronounced "breakthrough" which points to a missing characteristic bottleneck diameter. This indicates that there are many different-sized constrictions of transportation paths through the pore phase. In addition, the curves presented in Figure 8b exhibit that an increasing compaction load leads to a large number of constrictions concerning the pore phase. Thus, there exists a monotonous trend regarding the MIP-PSD in a sense that the curves are shifted gradually to the left for increasing densification.

A further characteristic which is used to quantitatively analyze bottlenecks of transportation paths through the pore phase is constrictivity. This characteristic is given by $\beta = (r_{min}/r_{max})^2$, where r_{max} and r_{min} are the radii for which c-PSD resp. MIP-PSD reach 50 % of the pore volume, see, e.g., Holzer et al. (2013b) and Stenzel et al. (2016) for details. Therefore, $r_{max} \geq r_{min}$ and $\beta \in [0, 1]$, where a value of 1 corresponds to no constrictions of transportation paths and lower values indicate a stronger occurrence of bottlenecks. Figure 9 visualizes the constrictivity as a function of the compaction load, where we can observe that β is monotonously decreasing for increasing compaction loads as expected. In other words, due to increasing compaction and the resulting densification of microstructure, transportation paths in through-plane direction become narrower or close complete. Therefore, some parts of the

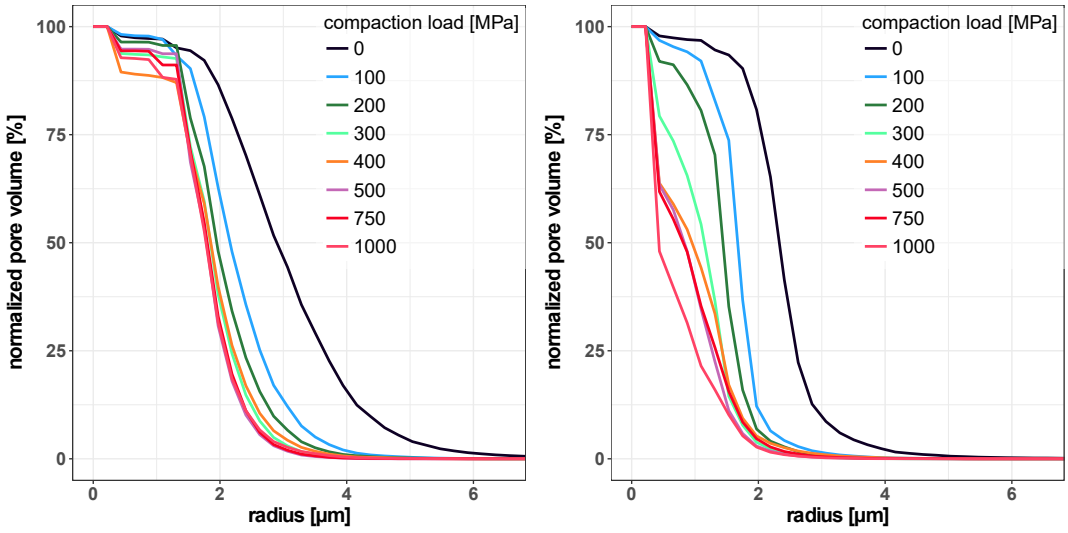

(a) Continuous pore size distribution

(b) MIP-PSD in through-plane direction

FIGURE 8 Two types of pore size distributions providing valuable information regarding the morphology of pore phase.

microstructure are hardly or no more accessible for transport through pore space.

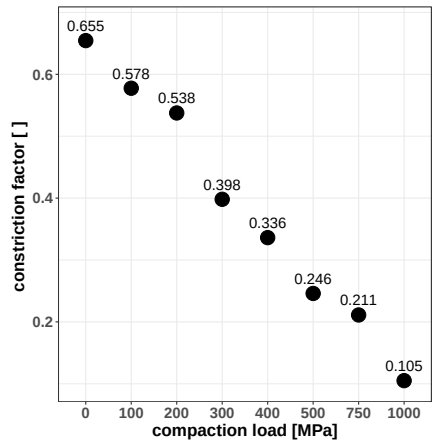

FIGURE 9 Constrictivity as a function of the compaction load.

Finally, in order to analyze and characterize the length of transportation paths through the pore phase, we investigate the relationship between the compaction load and the tortuosity of transportation paths. To be more precise, the distribution of geodesic tortuosity, see Stenzel et al. (2016, 2017), is computed by dividing the shortest path lengths through pore phase in through-plane direction by the thickness of the observation window. Further informa-

tion regarding different definitions of tortuosity can be found in Clennell (1997). The electrochemical importance of tortuosity with regard to effective transport processes is discussed in Holzer et al. (2013a). For an increasing compaction rate, the mean geodesic tortuosity rises, which corresponds to a shift of distributions to the right in Figure 10. This means that transportation paths through pore space get longer in higher compacted cathodes, which hinders ion transport from separator to current collector. Additionally, the wider distributions for larger compaction loads indicate that the lengths of shortest transportation path fluctuate more as a result of densification.

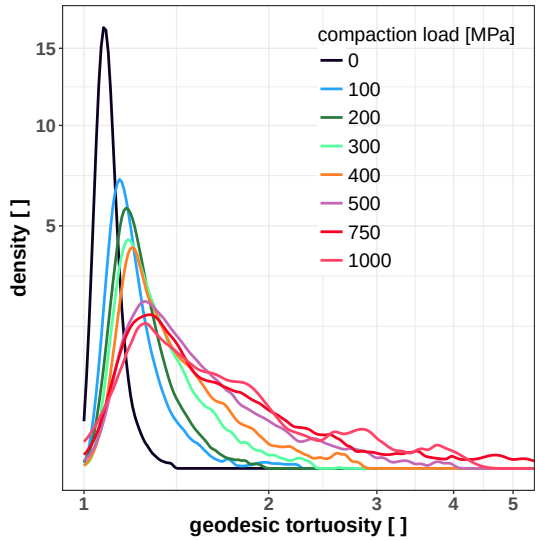

FIGURE 10 Distribution of geodesic tortuosity of transportation paths through pore phase in through-plane direction for different compaction loads.

3.3 | Particle-based characteristics

After having investigated phase-based image characteristics in Section 3.2, we now concentrate on image characteristics that are determined using the segmented 3D image data from Section 3.1, where every extracted NCM-particle of the considered microstructure can be accessed through its unique label. In particular, we will focus on the size distribution of NCM-particles and the distribution of their sphericity. Both characteristics are averaged over those 12 cutouts that have been described in Section 3.1.

To begin with, we are interested in the influence of increasing compaction loads on the particle size distribution, where we will use the volume-equivalent diameter in order to describe the size of the NCM-particles, i.e. the diameter of a sphere such that the volume of this sphere and the volume of the considered particle coincide. This way of characterizing the size of the particles is reasonable since the particles are nearly spherically shaped. Based on volume-equivalent diameters, we determine particle size distributions, see Figure 11. As it can be seen, the particle sizes range from about 2 to 20 μm, which almost coincides with the spectroscopic measurements (4 to 20 μm). In addition, an increasing compaction load leads to a relatively small reduction of the particle size, which will be further

quantified by the d_{50}-diameter.

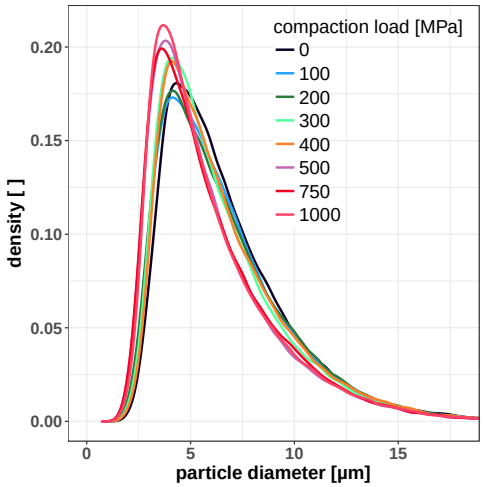

FIGURE 11 Particle size distribution for different compaction loads.

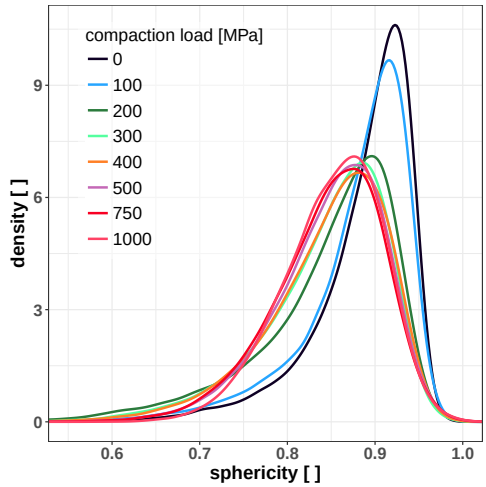

FIGURE 12 Sphericity distribution of NCM-particles for different compaction loads.

Another important characteristic is the so-called d_{50}-diameter, which is defined as the median of the particle size distribution. Table 3 shows the relationship between the d_{50}-diameter and the compaction load. The d_{50}-diameter of the uncompacted cathode, which is determined based on the segmentation of the NCM-particles, is given by 5.96 μm and therefore smaller than the experimentally determined d_{50}-diameter of approximately 7 μm, see Schmidt et al. (2018). This difference might be caused by cracked particles, which arise during the mixing procedure of cathode manufacturing, see Section 2.1. In general, an increase of the compaction load leads to slightly smaller particles, which is probably subject to particle cracking as well as compaction of the NCM-particles itselves when the internal porosity is reduced as a result of increasing compaction.

comp. load [MPa]	0	100	200	300	400	500	750	1000
d_{50}-diameter [μm]	5.96	5.85	5.81	5.61	5.75	5.15	5.19	5.14

TABLE 3 Median of the particle size distribution for different compaction loads.

We now focus on the investigation of the relationship between the compaction load and the distribution of sphericity of segmented NCM-particles. Figure 12 shows that there is a decrease of sphericity for increasing compaction loads. Especially the uncompacted and the 100 MPa compacted cathode exhibit a relatively high sphericity. However, in the range between 200 and 1000 MPa the increasing compaction seems to have nearly no influence on the sphericity as it can also be seen in Table 4. Since the values given in Table 4 are close to 1, we can conclude that the NCM-particles are almost spherically shaped, which coincides with the visual impression of Figure 3. Furthermore, the d_{50}-diameters of the 400 and 750 MPa compacted cathode seem to be too large since they violate the monotonous trend given by the remaining 6 samples. We suppose that this is caused by the fact that only one cathode sample of

each compaction load has been included in the tomographic imaging procedure and that the selected samples of the 400 and 750 MPa compacted cathode were a bit untypical. This conjecture will be additionally discussed in Section 4 with regard to the distribution of local porosities.

comp. load [MPa]	0	100	200	300	400	500	750	1000
mean sphericity	0.89	0.88	0.85	0.85	0.85	0.85	0.85	0.85

TABLE 4 Mean sphericity of NCM-particles as a function of the compaction load.

4 | PREDICTION OF MICROSTRUCTURAL CHARACTERISTICS USING PARAMETRIC PROBABILITY DISTRIBUTIONS

In this section we will consider parametric families of probability distributions to predict the distribution of two selected characteristics for different compaction loads. For this purpose, we first have to choose a suitable family of parametric probability distributions to model the considered quantity. Afterwards, we determine the maximum likelihood estimates (MLEs) of the parameters for all compaction loads. In a next step, we use classical regression analysis to predict the parameters for an arbitrary compaction load. In order to be able to validate this approach, we will not use several compaction loads in the regression step. Finally, we compare the predicted distribution with the distribution obtained by 3D image analysis.

Recall that in Section 3.2 we considered the minimum, maximum, mean and standard deviation of local porosities. At this point, we focus on the probability distribution of local porosities. Figure 13 shows results of the kernel density estimation of local porosities, which have been determined based on the preprocessed 3D image data. One can observe that due to the shape and the symmetry of the curves it is reasonable to model the distributions of local porosities by normal distributions. Therefore, the MLEs have been determined for all considered compaction loads. Table 5 shows the MLEs of the mean μ (denoted by $\hat{\mu}$) and the MLEs of the variance σ^2 (denoted by $\hat{\sigma}^2$), respectively. The variances of the 400 and the 750 MPa compacted cathode seem to be too high since they violate the monotonously decreasing trend, which is given by the remaining 6 samples. Since the 400 and the 750 MPa compacted cathode did not fit into the pattern given by the other samples with regard to the d_{50}-diameter, it is reasonable to assume that these two samples are a bit untypical for the respective compaction loads.

comp. load [MPa]	0	100	200	300	400	500	750	1000
$\hat{\mu}$	0.49	0.33	0.28	0.24	0.21	0.19	0.18	0.15
$1000 \cdot \hat{\sigma}^2$	4.02	2.41	2.22	2.04	2.52	1.83	2.03	1.54

TABLE 5 Maximum likelihood estimates of mean and variance.

At this point, we use classical least-square regression to predict mean and standard deviation as a function of the compaction load. In our case, we will not consider the 200 as well as the 300 MPa compacted cathode in this step, since these two samples will be used later as retained samples in order to be able to validate our approach. For both

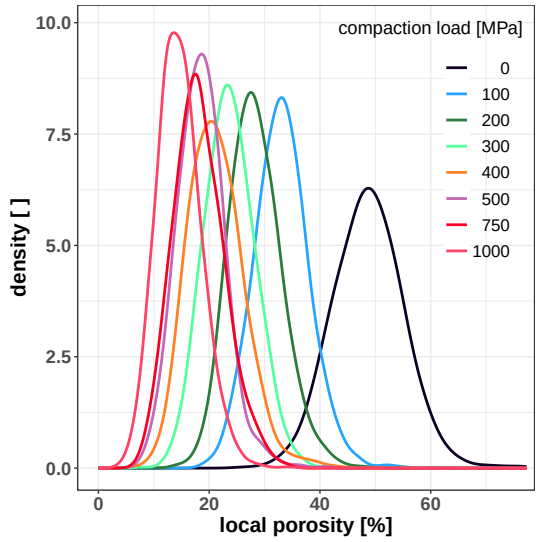

FIGURE 13 Kernel density estimation of local porosities for different compaction loads.

parameters, namely μ and σ^2, it turns out that using a rational function of the form

$$f(x) = \frac{ax + b}{x + d}$$

leads to reasonable fits, see Figure 14.

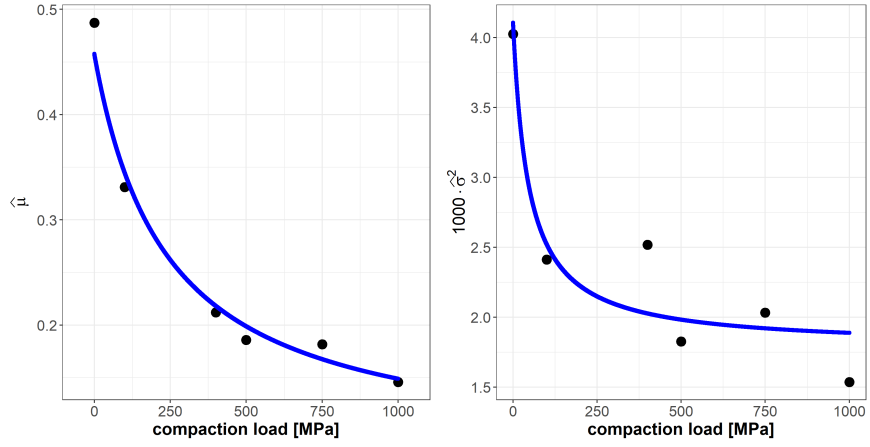

FIGURE 14 Least-square regression of mean (left) and variance (right) as a function of the compaction load. The black dots are the values obtained via maximum likelihood estimation.

This allows us to calculate the parameters of the normal distribution for each compaction load and therefore

we are able to predict the distribution of local porosities for an arbitrary compaction load. In particular, we obtain $\widetilde{\mu}_{200\,\mathrm{MPa}} = 0.283$, $\widetilde{\sigma}^2_{200\,\mathrm{MPa}} = 2.837 \cdot 10^{-3}$, $\widetilde{\mu}_{300\,\mathrm{MPa}} = 0.245$ and $\widetilde{\sigma}^2_{300\,\mathrm{MPa}} = 2.630 \cdot 10^{-3}$. Figure 15 compares the distribution of local porosities obtained from 3D image data as well as the distribution based on the regression approach for a compaction load of 200 and 300 MPa, respectively.

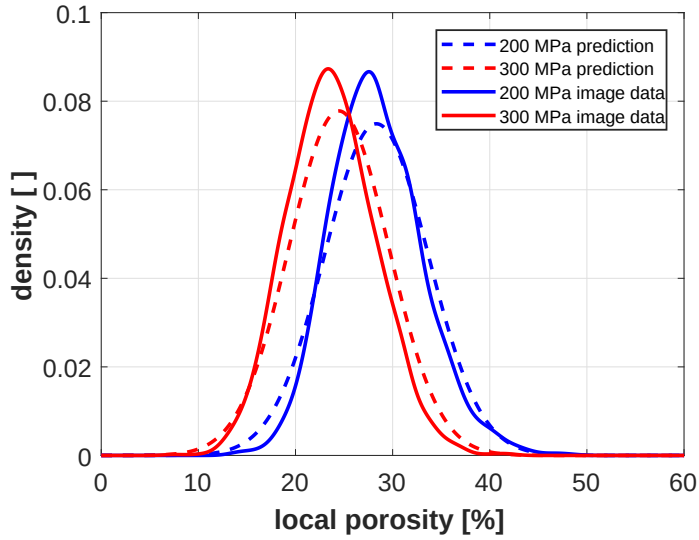

FIGURE 15 Distribution of local porosities obtained by 3D image data (solid lines) and by using the prediction based on the regression model (dashed lines) for 200 MPa (blue) and 300 MPa (red).

The previously described procedure can be analogously applied to other characteristics, which illustrates the flexibility of this approach. In the second part of this section, we consider the distribution of sphericity of NCM-particles. As it can be clearly seen in Figure 12, the family of normal distributions is no longer an appropriate choice. It turns out that the family of Burr distributions is suitable for modeling the distribution of $1 - X$, where X denotes the random sphericity of NCM-particles. The Burr distribution, or more formally the Burr Type XII distribution, is a continuous distribution with three parameters, namely a scale parameter $a > 0$ as well as two shape parameters $c > 0$ and $k > 0$, see Tadikamalla (1980). The cumulative distribution function F of the Burr distribution is given by

$$F(x) = \begin{cases} 1 - \left(1 + \left(\frac{x}{a}\right)^c\right)^{-k} & , \text{if } x \geq 0, \\ 0 & , \text{if } x < 0. \end{cases}$$

Analogously to the approach considered above for local porosities, we determine maximum likelihood estimates of the three parameters for each compaction load except for 400 MPa since this sample will be used later as retained sample for validation purposes. Afterwards, we consider each parameter estimate of the Burr distribution as a function of the compaction rate and fit a cubic polynomial using classical regression analysis. The result is shown in Figure 16. Therefore we are able to predict the parameters of the Burr distribution for a compaction load of 400 MPa, which are given by $\widetilde{a}_{400\,\mathrm{MPa}} = 0.182$, $\widetilde{c}_{400\,\mathrm{MPa}} = 3.305$, and $\widetilde{k}_{400\,\mathrm{MPa}} = 1.833$.

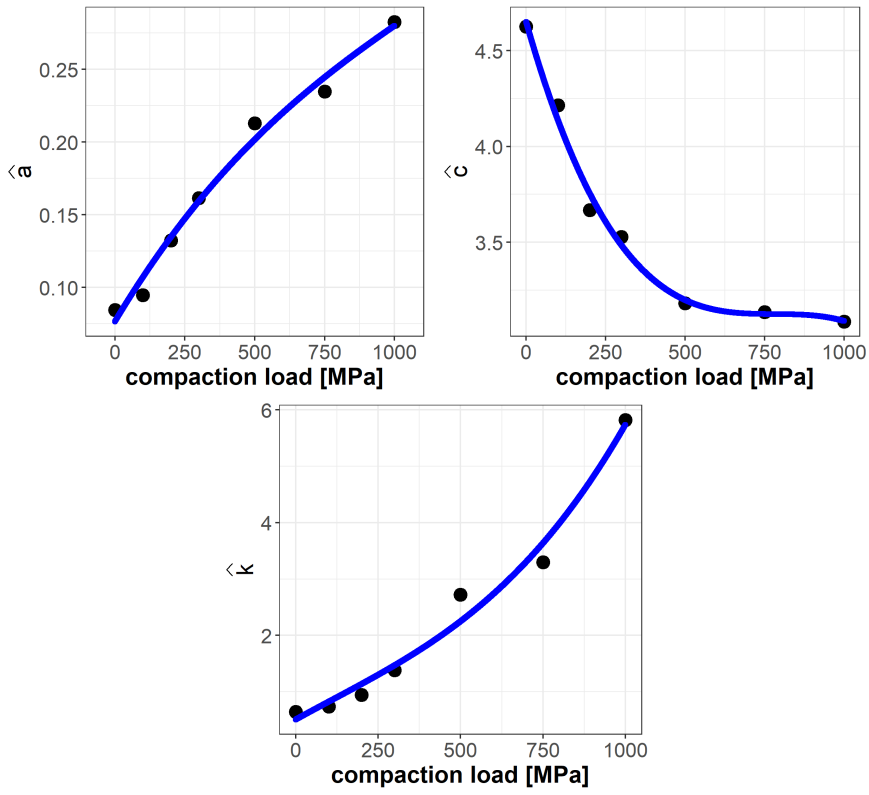

FIGURE 16 Least-square regression of scale parameter a (top left), shape parameter c (top right) and shape parameter k (bottom) of the Burr distribution by fitting a cubic polynomial based on the maximum likelihood estimates (black dots). Note that the 400 MPa compacted cathode is not included in the fitting procedure.

The resulting probability density function $f_{400\,\mathrm{MPa}}$ models the density of $1 - X$. In order to get the probability density function of the sphericity, denoted by $g_{400\,\mathrm{MPa}}$, we have to apply the transformation

$$g_{400\,\mathrm{MPa}}(x) = f_{400\,\mathrm{MPa}}(1 - x) \text{ for all } x \in [0, 1].$$

This allows us to predict the distribution of sphericity for a compaction load of 400 MPa. Figure 17 shows that both, the directly data-driven and the predicted distributions, coincide well and hence, this approach can be used to obtain a reliable prediction of the distribution of sphericity for an arbitrary compaction load in order to avoid the expensive cathode manufacturing process as well as the tomographic imaging procedure. Obviously, the previously described approach can be analogously applied to other image characteristics, as for example the distribution of geodesic tortuosities or the particle size distribution.

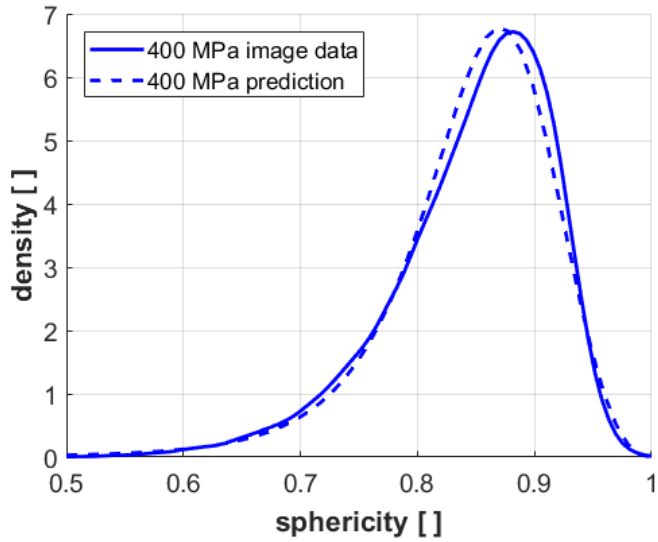

FIGURE 17 Distribution of the sphericity of NCM-particles based on 3D image data (solid lines) and by using the prediction based on the regression model (dashed lines) for 400 MPa.

5 | SUMMARY AND CONCLUSIONS

The aim of this work was the investigation of the relationship between the compaction load and the 3D microstructure of NCM-cathode films. For this purpose, eight differently compacted cathodes of the same material composition were manufactured and then imaged by synchrotron tomography. After preprocessing which, for example, encompasses an approach of artificially embedding binder and conductive additives into phase-segmented image data, several microstructural characteristics were computed based on the phase- and particle-segmented image data. Overall, there is a high accordance between the results from 3D image data and from experimental measurements. Almost all considered characteristics exhibit a monotonous behavior with regard to the compaction load. The global porosity, the constrictivity, the specific surface area per weight and the geometric tortuosity are monotonously decreasing for increasing compaction loads whereas the volume fraction of NCM-particles increases. Some quantities, as for example the sphericity or the thickness of the cathode, are subject to significant changes for relatively small compaction loads, whereas the influence of the compaction load on these characteristics is almost negligible for higher compaction loads. Almost all previously considered characteristics show that the most significant changes of the cathode morphology already occur for relatively small compaction rates (approximately up to 300 MPa). Moreover, compaction loads larger than 300 MPa lead to microstructural changes on a smaller scale. Note that these comparatively small changes of the cathode morphology can nonetheless imply significant changes with regard to the electrochemical performance. In Section 4 we used maximum likelihood estimation combined with regression analysis to predict the distribution of local porosities as well as sphericity of NCM-particles as a continuous function of the compaction load, which demonstrates the flexibility of our approach. We did not include the tomographic image data for certain compaction loads into the regression step in order to use them as retain samples for validation purposes. Due to the high accordance between the predicted distributions and the distributions based on 3D image data, it can be concluded that our approach is meaningful. Furthermore, the previously mentioned procedure can be used to predict the distribution of

several further microstructural characteristics as a function of the compaction load avoiding expensive manufacturing and imaging processes.

References

Beare, R. and Lehmann, G. (2006) The watershed transform in ITK - discussion and new developments. *The Insight Journal*, **6**.

Beucher, S. and Meyer, F. (1993) The morphological approach to segmentation: the watershed transformation. In *Mathematical Morphology in Image Processing* (ed. E. R. Dougherty), 433–481. New York: Marcel Dekker, Inc.

Bockholt, H., Haselrieder, W. and Kwade, A. (2013) Intensive dry and wet mixing influencing the structural and electrochemical properties of secondary lithium-ion battery cathodes. *ECS Transactions*, **50**, 25–35.

Bockholt, H., Indrikova, M., Netz, A., Golks, F. and Kwade, A. (2016) The interaction of consecutive process steps in the manufacturing of lithium-ion battery electrodes with regard to structural and electrochemical properties. *Journal of Power Sources*, **325**, 140–151.

Burger, W. and Burge, M. (2016) *Digital Image Processing: An Algorithmic Introduction Using Java*. London: Springer, 2nd edn.

Cho, S., Chen, C.-F. and Mukherjee, P. P. (2015) Influence of microstructure on impedance response in intercalation electrodes. *Journal of The Electrochemical Society*, **162**, A1202–A1214.

Clennell, M. B. (1997) Tortuosity: a guide through the maze. *Geological Society, London, Special Publications*, **122**, 299–344.

García, R. E., Chiang, Y.-M., Carter, W. C., Limthongkul, P. and Bishop, C. M. (2005) Microstructural modeling and design of rechargeable lithium-ion batteries. *Journal of The Electrochemical Society*, **152**, A255–A263.

Gnanaraj, J., Cohen, Y. S., Levi, M. and Aurbach, D. (2001) The effect of pressure on the electroanalytical response of graphite anodes and $LiCoO_2$ cathodes for Li-ion batteries. *Journal of Electroanalytical Chemistry*, **516**, 89–102.

Haselrieder, W., Ivanov, S., Christen, D. K., Bockholt, H. and Kwade, A. (2013) Impact of the calendering process on the interfacial structure and the related electrochemical performance of secondary lithium-ion batteries. *ESC Transactions*, **50**, 59–70.

Holzer, L., Iwanschitz, B., Hocker, T., Keller, L., Pecho, O. M., Sartoris, G., Gasser, P. and Muench, B. (2013a) Redox cycling of Ni–YSZ anodes for solid oxide fuel cells: Influence of tortuosity, constriction and percolation factors on the effective transport properties. *Journal of Power Sources*, **242**, 179–194.

Holzer, L., Wiedenmann, D., Münch, B., Keller, L., Prestat, M., Gasser, P., Robertson, I. and Grobéty, B. (2013b) The influence of constrictivity on the effective transport properties of porous layers in electrolysis and fuel cells. *Journal of Materials Science*, **48**, 2934–2952.

Hoshen, J. and Kopelman, R. (1976) Percolation and cluster distribution. I. Cluster multiple labeling technique and critical concentration algorithm. *Physical Review B*, **14**, 3438–3445.

Huang, X., Tu, J., Xia, X., Wang, X., Xiang, J., Zhang, L. and Zhou, Y. (2009) Morphology effect on the electrochemical performance of NiO films as anodes for lithium ion batteries. *Journal of Power Sources*, **188**, 588 – 591.

Kuchler, K., Westhoff, D., Feinauer, J., Mitsch, T., Manke, I. and Schmidt, V. (2018) Stochastic model for the 3D microstructure of pristine and cyclically aged cathodes in Li-ion batteries. *Modelling and Simulation in Materials Science and Engineering*, **26**, 035005.

Lenze, G., Bockholt, H., Schilcher, C., Froböse, L., Jansen, D., Krewer, U. and Kwade, A. (2018) Impacts of variations in manufacturing parameters on performance of Lithium-Ion-Batteries. *Journal of The Electrochemical Society*, **165**, A314–A322.

Lenze, G., Röder, F., Bockholt, H., Haselrieder, W., Kwade, A. and Krewer, U. (2017) Simulation-supported analysis of calendering impacts on the performance of Lithium-Ion-Batteries. *Journal of The Electrochemical Society*, **164**, A1223–A1233.

Li, W. and Currie, J. C. (1997) Morphology effects on the electrochemical performance of $LiNi_{1-x}Co_xO_2$. *Journal of The Electrochemical Society*, **144**, 2773–2779.

Lim, C., Yan, B., Kang, H., Song, Z., Chao Lee, W., De Andrade, V., De Carlo, F., Yin, L., Kim, Y. and Zhu, L. (2016) Analysis of geometric and electrochemical characteristics of lithium cobalt oxide electrode with different packing densities. *Journal of Power Sources*, **328**, 46–55.

Machado Charry, E., Neumann, M., Lahti, J., Schennach, R., Schmidt, V. and Zojer, K. (2018) Pore space extraction and characterization of sack paper using μ-CT. *Journal of Microscopy*. In print.

Meyer, C., Bockholt, H., Haselrieder, W. and Kwade, A. (2017) Characterization of the calendering process for compaction of electrodes for lithium-ion batteries. *Journal of Materials Processing Technology*, **249**, 172 – 178.

Münch, B. and Holzer, L. (2008) Contradicting geometrical concepts in pore size analysis attained with electron microscopy and mercury intrusion. *Journal of the American Ceramic Society*, **91**, 4059–4067.

Röder, F., Sonntag, S., Schröder, D. and Krewer, U. (2016) Simulating the impact of particle size distribution on performance of graphite electrodes in Lithium-Ion batteries. *Energy Technology*, **4**, 1588–1597.

Schmidt, D., Kamlah, M. and Knoblauch, V. (2018) Highly densified NCM-cathodes for high energy Li-ion batteries: Microstructural evolution during densification and its influence on the performance of the electrodes. *Journal of Energy Storage*, **17**, 213–223.

Shin, Y. and Manthiram, A. (2004) Influence of microstructure on the electrochemical performance of $LiMn_{2-y-z}Li_yNi_zO_4$ spinel cathodes in rechargeable lithium batteries. *Journal of Power Sources*, **126**, 169 – 174.

Soille, P. (2003) *Morphological Image Analysis: Principles and Applications*. New York: Springer, 2nd edn.

Song, T., Xia, J., Lee, J.-H., Lee, D. H., Kwon, M.-S., Choi, J.-M., Wu, J., Doo, S. K., Chang, H., Park, W. I., Zang, D. S., Kim, H., Huang, Y., Hwang, K.-C., Rogers, J. A. and Paik, U. (2010) Arrays of sealed silicon nanotubes as anodes for lithium ion batteries. *Nano Letters*, **10**, 1710–1716.

Spettl, A., Wimmer, R., Werz, T., Heinze, M., Odenbach, S., Krill III, C. E. and Schmidt, V. (2015) Stochastic 3D modeling of Ostwald ripening at ultra-high volume fractions of the coarsening phase. *Modelling and Simulation in Materials Science and Engineering*, **23**, 065001.

Stenzel, O., Pecho, O. M., Holzer, L., Neumann, M. and Schmidt, V. (2016) Predicting effective conductivities based on geometric microstructure characteristics. *AIChE Journal*, **62**, 1834–1843.

— (2017) Big data for microstructure-property relationships: A case study of predicting effective conductivities. *AIChE Journal*, **63**, 4224–4232.

Tadikamalla, P. R. (1980) A look at the Burr and related distributions. *International Statistical Review*, **48**, 337–344.

Vu, A., Qian, Y. and Stein, A. (2012) Porous electrode materials for lithium-ion batteries-how to prepare them and what makes them special. *Advanced Energy Materials*, **2**, 1056–1085.

Waldmann, T., Iturrondobeiti, A., Kasper, M., Ghanbari, N., Aguesse, F., Bekaert, E., Daniel, L., Genies, S., Gordon, I. J., Löble, M. W., Vito, E. D. and Wohlfahrt-Mehrens, M. (2016) Review—post-mortem analysis of aged lithium-ion batteries: Disassembly methodology and physico-chemical analysis techniques. *Journal of The Electrochemical Society*, **163**, A2149–A2164.

Wang, Y., Zhang, W., Chen, L., Shi, S. and Liu, J. (2017) Quantitative description on structure-property relationships of Li-ion battery materials for high-throughput computations. *Science and Technology of Advanced Materials*, **18**, 134–146.

Wang, Z., Zhou, L. and (David) Lou, X. W. (2012) Metal oxide hollow nanostructures for lithium-ion batteries. *Advanced Materials*, **24**, 1903–1911.

Weisenberger, C., Guth, G., Bernthaler, T. and Knoblauch, V. (2014) New quality evaluation approaches for lithium ion batteries using the interference layer metallography in combination with quantitative structural analysis. *Practical Metallography*, **51**, 5–31.

Wiedemann, A. H., Goldin, G. M., Barnett, S. A., Zhu, H. and Kee, R. J. (2013) Effects of three-dimensional cathode microstructure on the performance of lithium-ion battery cathodes. *Electrochimica Acta*, **88**, 580–588.

Zhang, H., Yu, X. and Braun, P. V. (2011) Three-dimensional bicontinuous ultrafast-charge and -discharge bulk battery electrodes. *Nature Nanotechnology*, **6**, 277–281.

Zheng, H., Liu, G., Song, X. and Battaglia, V. (2008) $Li[Ni_{1/3}Mn_{1/3}Co_{1/3}]O_2$-based electrodes for PHEV applications: An optimization. *ECS Transactions*, **11**, 1–9.

Zheng, H., Tan, L., Liu, G., Song, X. and Battaglia, V. S. (2012) Calendering effects on the physical and electrochemical properties of $Li[Ni_{1/3}Mn_{1/3}Co_{1/3}]O_2$ cathode. *Journal of Power Sources*, **208**, 52–57.